Electronic supplementary materials *Mendeleev Commun.*, 2025, **35**, 169–171

Polyfluorinated Blatter radicals

Dmitry A. Gulyaev, Nurlan V. Gadimov, Nina P. Gritsan, Evgeny M. Kadilenko, Pavel G. Shangin, Mikhail A. Syroeshkin, Egor A. Sosunov and Evgeny V. Tretyakov

Syntheses of Compounds

4-Fluorobenzoyl chloride. In a Schlenk flask, thionyl chloride (8 ml, 110.1 mmol) was added to 4-fluorobenzoic acid (2 g, 14.3 mmol) under an argon atmosphere. The resulting solution was kept under vigorous stirring at 73 °C. An excess amount of $SOCl_2$ was removed in vacuum to give a crude title product, which was used without further purification.

4-Fluoro-*N*-phenylbenzamide. In a Schlenk flask, aniline (1.46 g, 15.73 mmol) and triethylamine (1.41 g, 14.3 mmol) were sequentially added to 4-fluorobenzoyl chloride (2 g, 14.3 mmol) at 0 °C in an argon atmosphere. The reaction mixture was stirred for 24 hours at room temperature. The product was extracted from the resulting suspension with chloroform (2×10 ml), and the combined extracts were evaporated in vacuum. The residue was recrystallized from a mixture of chloroform with ethyl acetate (3:1). Yield of 70%, colorless crystals. ^{1}H NMR (300 MHz, DMSO-d_6) δ: 7.07–7.17 (m, 1H), 7.31–7.45 (m, 4H), 7.78 (d, 2H, *J* 8.06 Hz), 8.06 (dd, 2H, *J* 8.43, 5.68 Hz), 10.28 (s, 1H). ^{13}C NMR (75 MHz, DMSO-d_6) δ: 114.93–115.61, 120.40, 123.71, 128.59, 130.36 (d, J 9.40 Hz), 131.36, 139.05, 162.39. ^{19}F NMR (282 MHz, DMSO-d_6) δ: –109.65 (s, 1F).

4-Fluoro-*N*-phenylbenzimidoyl chloride. A solution of 4-fluoro-*N*-phenylbenzamide (3.27 g, 15.23 mmol) in $SOCl_2$ (8.85 ml, 8 eq.) was heated at 70 °C for 4 hours in an argon atmosphere. An excess amount of $SOCl_2$ was removed in vacuum to give a crude title product in form of a greenish solid (3.41 g, 96% yield), which was used without further purification.

3-(4-Fluorophenyl)-1-(2,3,6-trifluorophenyl)-1,4-dihydrobenzo[*e*][1,2,4]triazine-4-yl (1a). 2,3,6-Trifluorophenylhydrazine (0.29 g, 1.79 mmol) and triethylamine (0.18 g, 1.79 mmol) were sequentially added to a stirred solution of 4-fluoro-*N*-phenylbenzimidoyl chloride (0.42 g, 1.79 mmol) in dry THF (3 ml) at –15 °C in an argon atmosphere. The reaction mixture was stirred for 24 hours at room temperature, then diluted with CH_2Cl_2 (25 ml) and treated with a 2% aqueous solution of acetic acid (2×10 ml). The organic layer was separated, dried over Na_2SO_4 and concentrated in vacuum.

The obtained amidrazone (0.333 g, 0.93 mmol) was dissolved in CH_2Cl_2 (4 ml), to the solution MnO_2 (0.80 g, 9.3 mmol) was added, and the reaction mixture was stirred for 30 hours at room temperature. The mixture was filtered through a thin layer of aluminum oxide, and the resulting solution was concentrated in vacuum. The residue was purified by silica gel column chromatography (petroleum ether/ethyl acetate [9:1], R_f = 0.5). Yield 0.213 g (35%), mp 178.2–178.6°C. IR (KBr, ν/cm^{-1}): 3436 (w), 3077 (w), 2959 (w), 2930 (w), 2544 (w), 2429 (w), 2236 (w), 2028 (w), 1915 (w), 1844 (w), 1785 (w), 1723 (w), 1632 (w), 1599 (m), 1505 (s), 1478 (s), 1392 (s). HRMS (ESI), *m*/*z*: 356.0804 $[M]^+$, (calc. for $C_{19}H_{10}F_4N_3^+$, *m*/*z*: 356.0805).

3-(4-Fluorophenyl)-1-(2,3,5,6-tetrafluorophenyl)-1,4-dihydrobenzo[*e*][1,2,4]triazine-4-yl (1b). 2,3,5,6-Tetrafluorophenylhydrazine (0.322 g, 1.79 mmol) and triethylamine (0.18 g, 1.79 mmol) were sequentially added to a stirred solution of 4-fluoro-*N*-phenylbenzimidoyl chloride (0.42 g, 1.79 mmol) in dry THF (3 ml) at –15 °C in an argon atmosphere. The reaction mixture was stirred for 24 hours at room temperature, then diluted with CH_2Cl_2 (25 ml) and treated with a 2% aqueous solution of acetic acid (2×10 ml). The organic layer was separated, dried over Na_2SO_4 and concentrated in vacuum.

The obtained amidrazone (0.351 g, 0.93 mmol) was dissolved in CH_2Cl_2 (4 ml), to the solution MnO_2 (0.80 g, 9.3 mmol) was added, and the reaction mixture was stirred for 6 hours at room temperature. The mixture was filtered through a thin layer of aluminum oxide and the resulting solution was concentrated in vacuum. The residue was purified by silica gel column chromatography (petroleum ether/ethyl acetate [9:1], R_f = 0.5). Yield 0.280 g (40%), mp 217.2–217.8 °C. IR (KBr, ν/cm^{-1}): 3432 (w), 3092 (w), 2799 (w), 2584 (w), 2528 (w), 2409 (w), 2352 (w), 2251 (w), 2031 (w), 1967 (w), 1911 (w), 1789 (w), 1641 (m), 1621 (m), 1599 (s), 1517(s), 1476 (s), 1390 (s). HRMS (ESI), *m*/*z*: 375.0784 $[M+H]^+$, (calc. for $C_{19}H_9F_5N_3^+$, 375.0789).

3-(4-Fluorophenyl)-1-(2,3,4,5,6-pentafluorophenyl)-1,4-dihydrobenzo[*e*][1,2,4]triazine-4-yl (1c). 2,3,4,5,6-Pentafluorophenylhydrazine (0.354 g, 1.79 mmol) and triethylamine (0.18 g, 1.79 mmol) were sequentially added to a stirred solution of 4-fluoro-*N*-phenylbenzimidoyl chloride (0.42 g, 1.79 mmol) in dry THF (3 ml) at –15 °C in an argon atmosphere. The reaction mixture was stirred for 24 hours at room temperature, then diluted with CH_2Cl_2 (25 ml) and treated with a 2% aqueous solution of acetic acid (2×10 ml). The organic layer was separated, dried over Na_2SO_4 and concentrated in vacuum.

The obtained amidrazone (0.367 g, 0.93 mmol) was dissolved in CH_2Cl_2 (4 ml), to the solution MnO_2 (0.80 g, 9.3 mmol) was added, and the reaction mixture was stirred for 6 hours at room temperature. The mixture was filtered through a thin layer of aluminum oxide and the resulting solution was concentrated in vacuum. The residue was purified by silica gel column chromatography (petroleum ether/ethyl acetate [9:1], R_f = 0.5). Yield 0.277 g (0.71 mmol (38%), mp 182.2–182.6 °C. IR (KBr, ν/cm^{-1}): 3443 (w), 3070 (w), 2978 (w), 2884 (w), 2835 (w), 2663 (w), 2586 (w), 2490 (w), 2446 (w), 2383 (w), 2036 (w), 1917 (w), 1787 (w), 1599 (m), 1513 (s), 1487 (s), 1461 (m), 1391(s). HRMS (ESI), *m*/*z*: 392.0607 $[M]^+$, (calc. for $C_{19}H_8F_6N_3^+$, 392.0617).

X-Ray Diffractometry

Table S1. Crystallographic data and structure refinement details for **1a**, **1b**, **1c**.

Identification code	**1a**	**1b**	**1c**
X-Ray source type	diffractometer	diffractometer	diffractometer
Empirical formula	$C_{19}H_{10}F_4N_3$	$C_{19}H_9F_5N_3$	$C_{19}H_8F_6N_3$
Formula weight	356.30	374.29	392.28
Temperature, K	100(2)	200(2)	100(2)
Color	black	black	black
Crystal size, mm	0.170×0.090×0.050	0.210×0.060×0.040	0.140×0.070×0.050
Wavelength, Å	0.71073	1.54178	0.71073
Crystal system	Monoclinic	Monoclinic	Triclinic
Space group	*Pc*	$P2_1$	*P*-1
a, Å	7.6749(9)	7.72710(10)	7.5444(4)
b, Å	13.2865(15)	29.9761(5)	13.4606(5)
c, Å	29.611(3)	13.2726(2)	15.7307(8)
α, deg.	90	90	102.175(2)
β, deg.	96.469(4)	91.0326(9)	96.784(3)
γ, deg.	90	90	91.454(3)
V, Å3	3000.3(6)	3073.81(8)	1548.54(13)
Z	8	8	4
Density (calc.), Mg/mm^3	1.578	1.618	1.683
μ, mm^{-1}	0.131	1.229	0.153
F(000)	1448	1512	788
Theta range, deg.	1.533–26.376	2.948–74.000	1.815–25.179
Index ranges	–8 ≤ h ≤ 9, –16 ≤ k ≤ 16, –33 ≤ l ≤ 36	–9 ≤ h ≤ 9, –36 ≤ k ≤ 36, –16 ≤ l ≤ 16	–9 ≤ h ≤ 9, –16 ≤ k ≤ 16, –7 ≤ l ≤ 18
Reflections collected	30753	38954	5508
Independent reflections	9337 (R_{int} = 0.0884)	11522 (R_{int} = 0.0815)	5508 (R_{int} = 0.0637)
Data/restraints/parameters	9337/2/967	11522 / 1 / 974	5508/0/506
R_1/*wR2* ($I > 2\sigma(I)$)	R_1 = 0.0657, wR_2 = 0.1497	R_1 = 0.0575, wR_2 = 0.1610	R_1 = 0.0601, wR_2 = 0.1220
R_1/*wR2* (all data)	R_1 = 0.0955, wR_2 = 0.1688	R_1 = 0.0660, wR_2 = 0.1690	R_1 = 0.1331, wR_2 = 0.1477
Goodness-of-fit on F^2	1.065	1.043	0.993
Largest diff. peak and hole	0.312/–0.284	0.380/–0.454	0.290/–0.298

Initial determination of unit cell parameters, refinement, and integration of reflection intensities were performed in the Bruker APEX3 software.[S1] Absorption corrections for the experimental reflection intensities were applied using the SADABS software.[S2] Crystal structures of **1a**, **1b**, and **1c** were solved by direct methods[S3] and refined by the full-matrix least-squares technique on F^2 using the OLEX2 structural data visualization and analysis software suite.[S4,S5] All nonhydrogen atoms were refined with anisotropic thermal parameters.

Refinement of geometrical coordinates and atomic displacement parameters of a fluorine atom disordered over two positions in structure 1a was performed without any constrains or restrains. All hydrogen atoms were derived from the Fourier synthesis map and refined isotopically with dependent isotropic thermal parameters with $U_{iso}(H) = 1.2U_{eq}(C)$, while hydrogen-bonding H atoms in structures **1a–c** were refined without additional restraints.

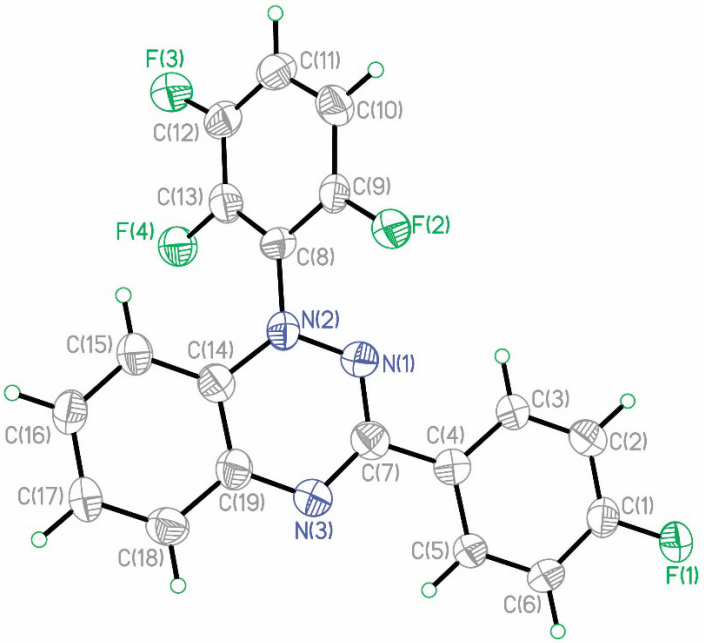

Figure S1. An ORTEP diagram of polyfluorinated radical **1a** at the 50% probability level and a crystallographic numbering scheme of non-hydrogen selected atoms.

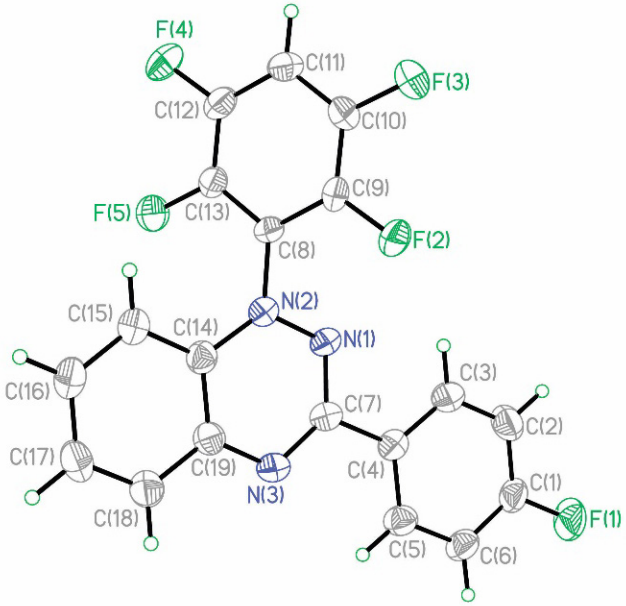

Figure S2. An ORTEP diagram of polyfluorinated radical **1b** at the 50% probability level and a crystallographic numbering scheme of non-hydrogen selected atoms.

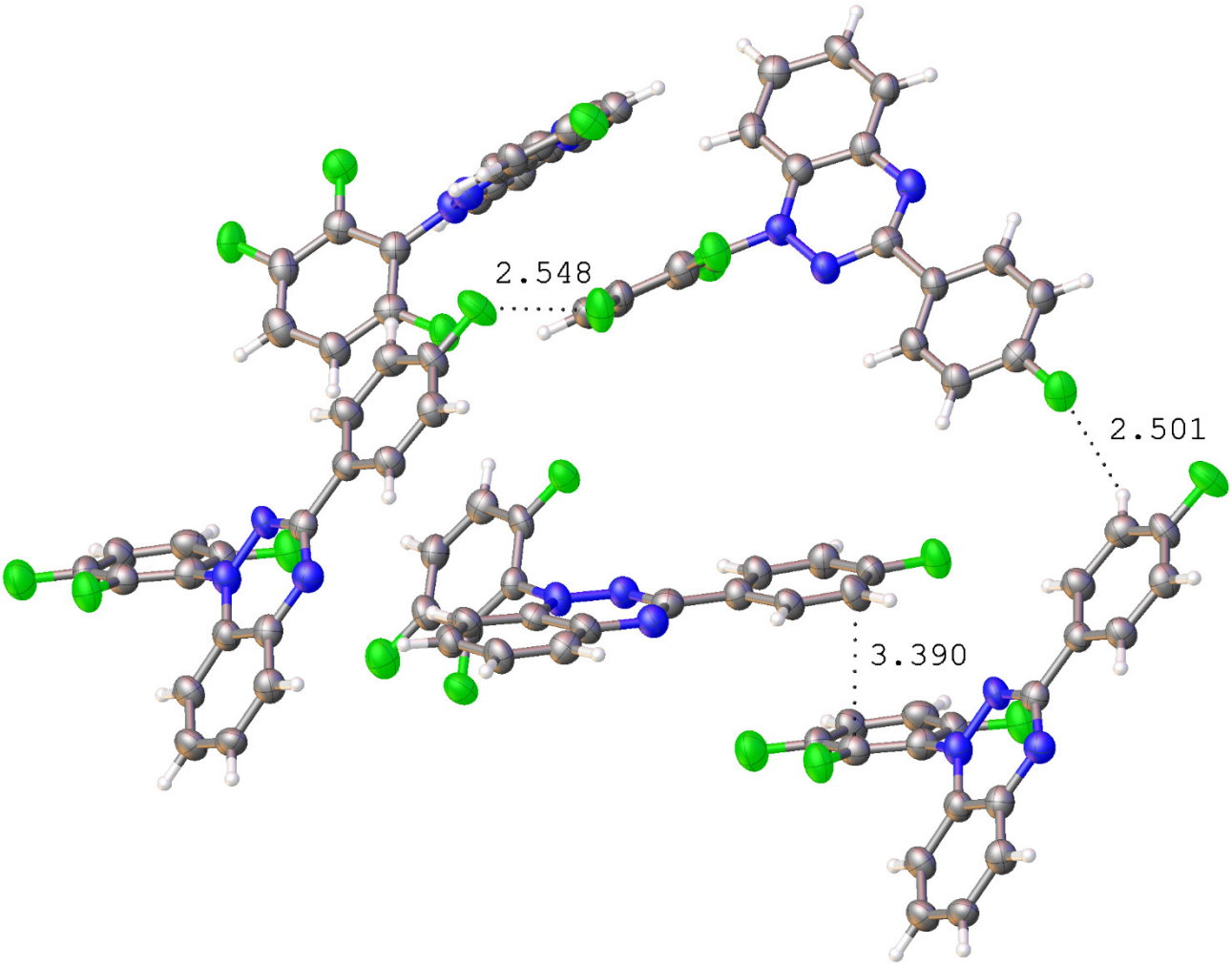

Figure S3. Short contacts in structure of **1a**.

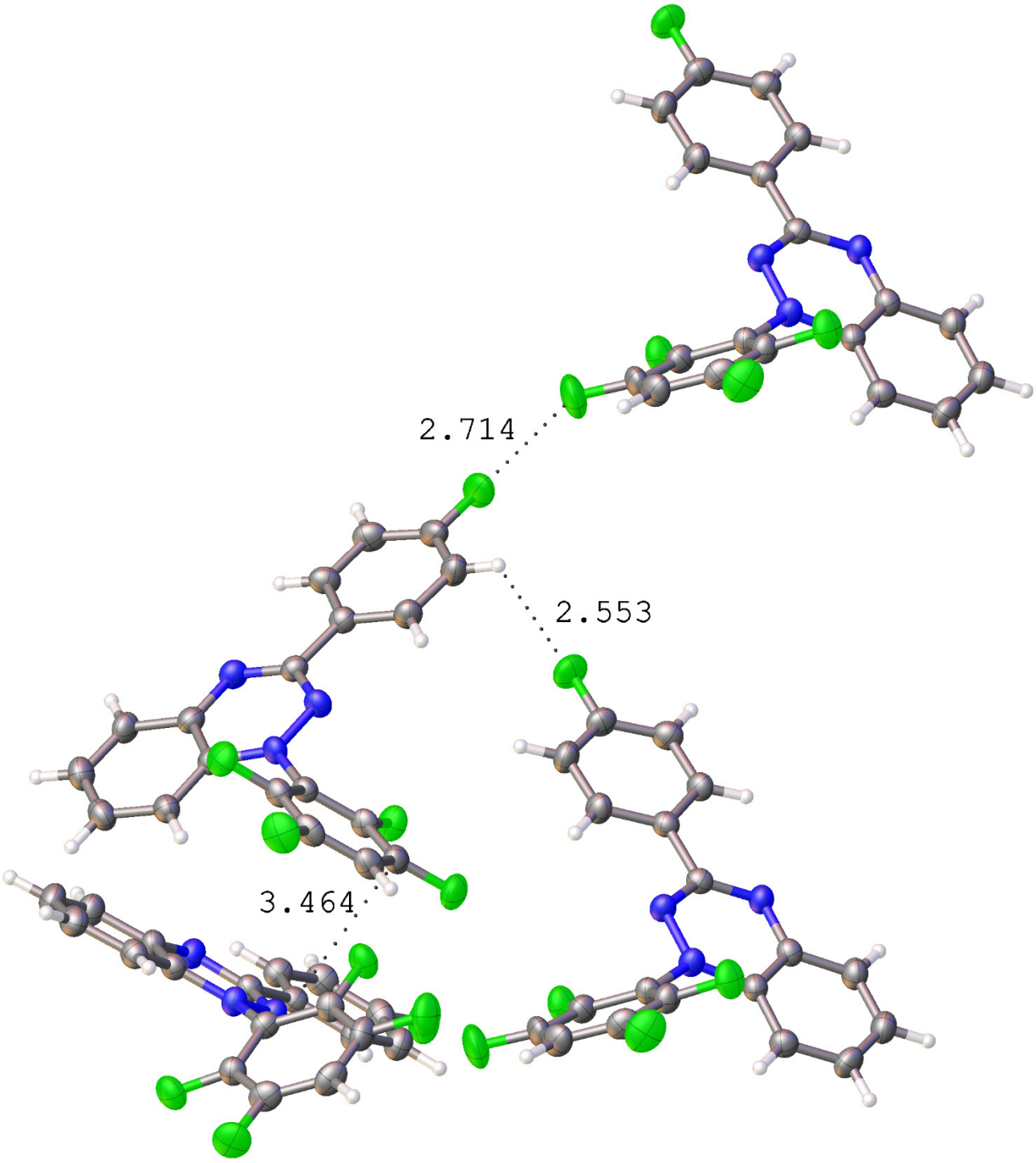

Figure S4. Short contacts in structure of **1b**.

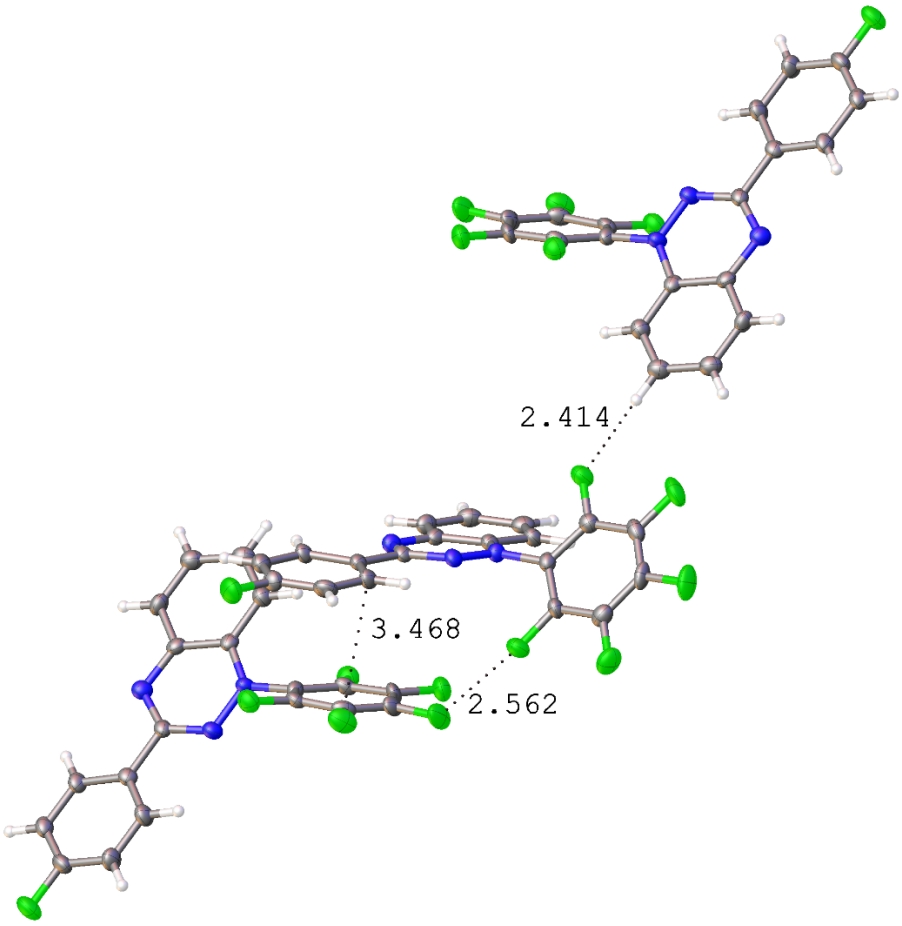

Figure S5. Short contacts in structure of **1c**.

Table S2. Selected bond lengths (Å) and torsion angles (°) for **1a**, **1b**, and **1c**.

D(X-Y)	**1a**	**1b**	**1c**
C(14)-C(15)	1.398(10)	1.396(7)	1.391(5)
C(15)-C(16)	1.367(10)	1.383(8)	1.377(6)
C(16)-C(17)	1.397(10)	1.408(9)	1.401(6)
C(17)-C(18)	1.371(10)	1.376(8)	1.378(6)
C(18)-C(19)	1.401(10)	1.398(8)	1.391(6)
C(14)-C(19)	1.417(9)	1.418(7)	1.430(5)
N(2)-C(14)	1.396(8)	1.398(6)	1.384(5)
N(1)-N(2)	1.365(7)	1.367(6)	1.372(4)
N(1)-C(7)	1.337(9)	1.324(7)	1.338(5)
N(3)-C(7)	1.343(9)	1.345(7)	1.332(5)
N(3)-C(19)	1.381(9)	1.366(7)	1.380(5)
α(X-Y-Z-U)	**1a**	**1b**	**1c**
N(1)-N(2)-C(8)-C(9)	-52.9(8)	-51.8(6)	-51.0(5)
C(3)-C(4)-C(7)-N(3)	-177.0(7)	-177.3(5)	-172.1(4)

Cyclic Voltammetry

The redox behavior of the compounds was analyzed by cyclic voltammetry using an IPC-Pro-MF digital potentiostat (Econix). The measurements were performed in a glove box in argon atmosphere at humidity and oxygen levels not exceeding 0.1 ppm in a standard three-electrode glass cell at a potential scan rate of 0.025–1.00 $V \cdot s^{-1}$. The working electrode was a glassy carbon disk electrode with a disk diameter of 1.7 mm; the auxiliary electrode was a Pt wire; the reference electrode was an Ag wire coated with AgCl; the reference electrode was calibrated relative to the Fc/Fc^+ pair; the background electrolyte was a 0.1 M solution of Bu_4NPF_6 in MeCN with a water content not exceeding 20 ppm or in DMF with a water content not exceeding 40 ppm. UV-vis spectroscopy was performed on an Agilent 8453 instrument. The spectra were registered in a 10 mm quartz cell with a PTFE stopper. Solutions of compounds were prepared in a glove box.

Table S3. Potentials (in mV *vs*. Ag/AgCl) of the forward (fw) and reverse (rev) peaks of the voltammetric curves for the reduction (red) and oxidation (ox) of compounds **1a**, **1b** and **1c** on a glassy carbon electrode in 0.1 M Bu_4NPF_6/MeCN and DMF, obtained by approximating to zero current the peak potential – peak current dependences for the curves recorded at 25, 50, 100, 200, 500 and 1000 $mV \cdot s^{-1}$; the potential differences of the forward and reverse peaks and the half-wave potential values.

Compound	solvent	$E_{fw}^{p,red}$	$E_{rev}^{p,red}$	$\Delta E^{p,red}$	$E_{1/2}^{red}$	$E_{fw}^{p,ox}$	$E_{rev}^{p,ox}$	$\Delta E^{p,ox}$	$E_{1/2}^{ox}$
1a	MeCN	–989	–920	69	**–954**	263	199	64	**231**
	DMF	–984	–919	65	**–952**	274	207	67	**240**
1b	MeCN	–929	–862	67	**–896**	303	236	67	**270**
	DMF	–967	–900	67	**–934**	267	200	67	**234**
1c	MeCN	–919	–856	63	**–888**	312	245	67	**278**
	DMF	–918	–852	66	**–885**	308	242	66	**275**

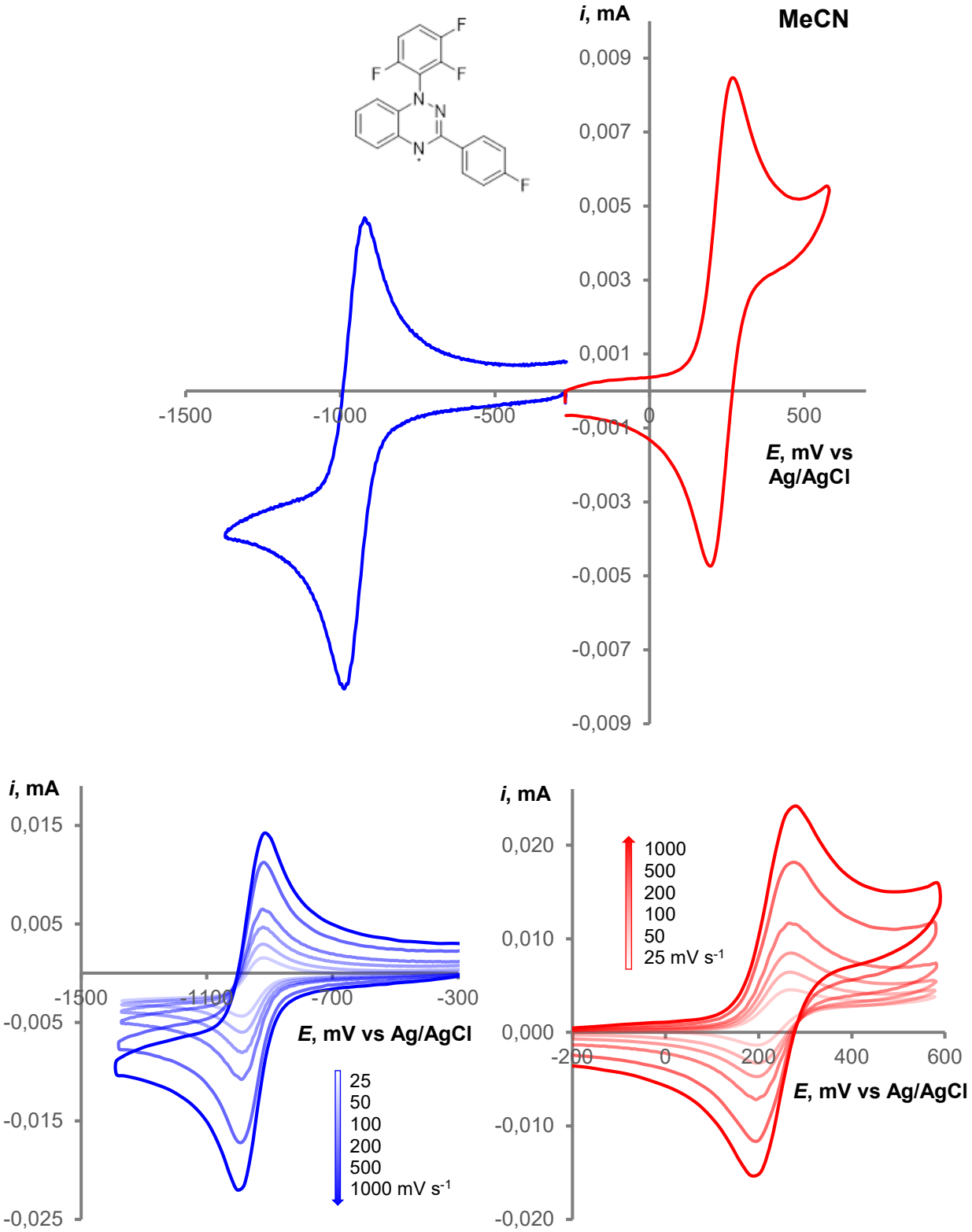

Figure S6. CV curves of reduction (*blue*) and oxidation (*red*) of $1 \cdot 10^{-3}$ mol dm^{-3} of **1a** in 0.1 M Bu_4NPF_6/MeCN on a glassy carbon disk working electrode (d = 1.7 mm) at a potential scan rate of 100 mV·s^{-1} (*top*) and 25, 50, 100, 200, 500 and 1000 mV·s^{-1} (*bottom*). Temperature 298 K.

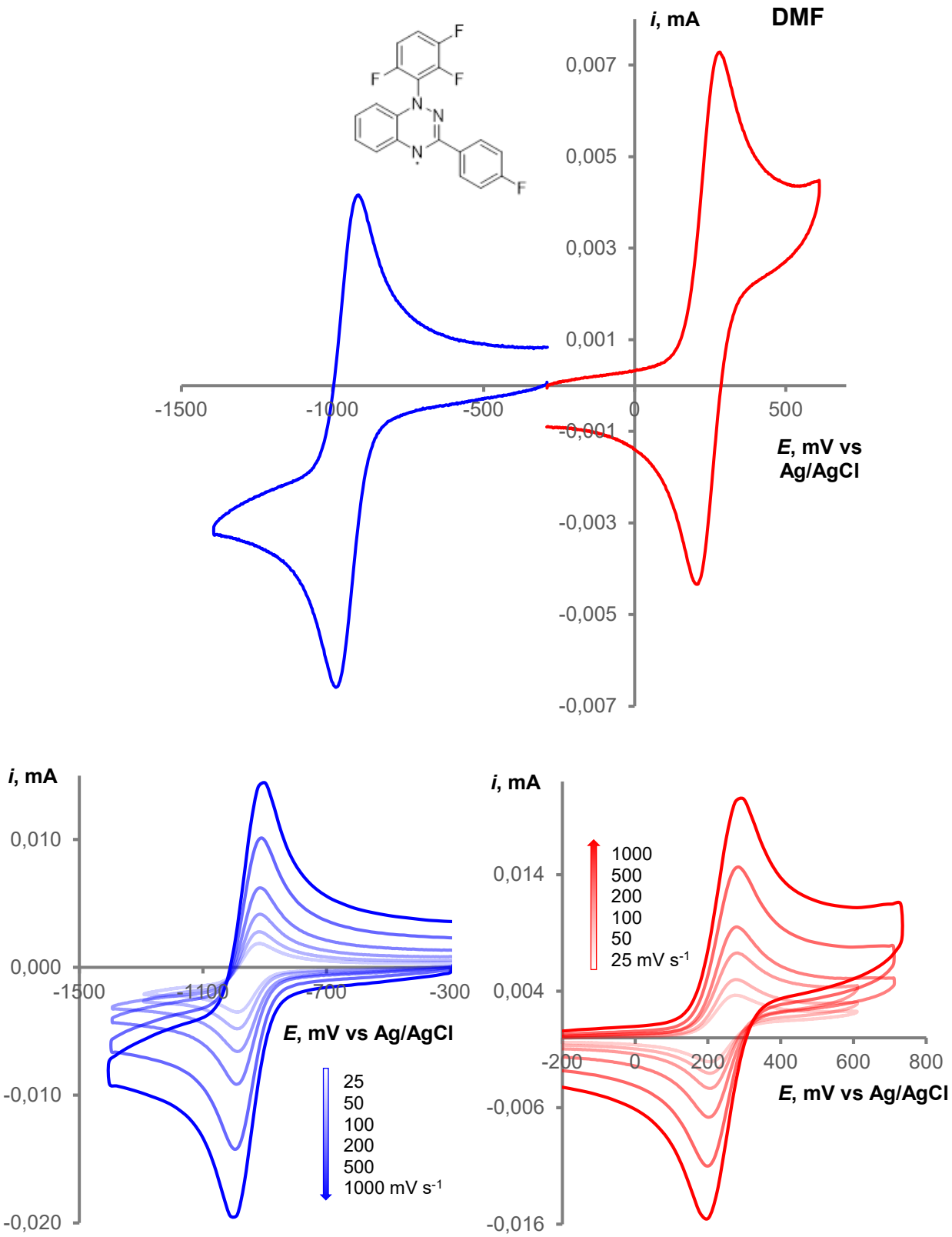

Figure S7. CV curves of reduction (*blue*) and oxidation (*red*) of $1 \cdot 10^{-3}$ mol dm^{-3} of **1a** in 0.1 M Bu_4NPF_6/DMF on a glassy carbon disk working electrode (d = 1.7 mm) at a potential scan rate of 100 mV·s^{-1} (*top*) and 25, 50, 100, 200, 500 and 1000 mV·s^{-1} (*bottom*). Temperature 298 K.

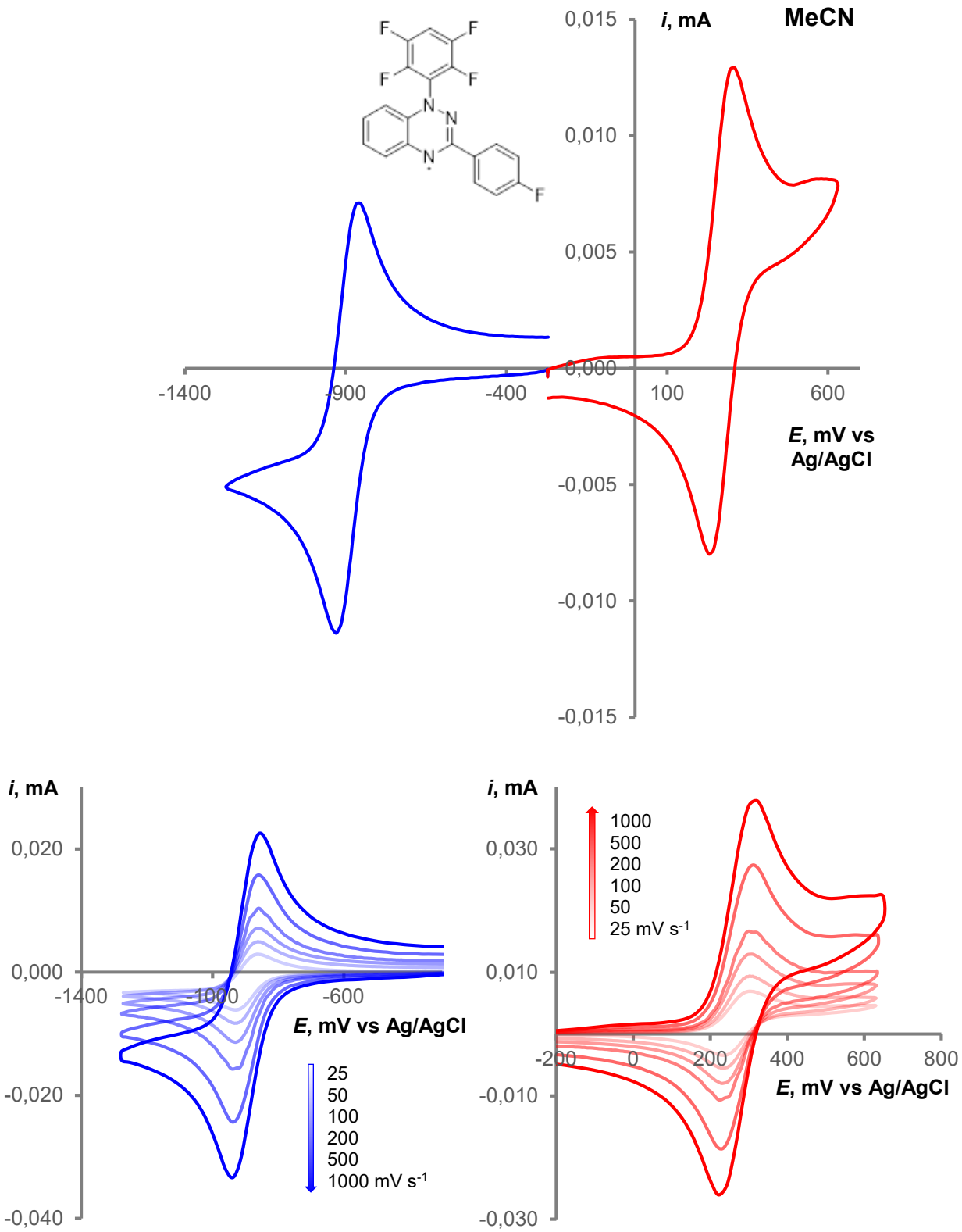

Figure S8. CV curves of reduction (*blue*) and oxidation (*red*) of $1.5 \cdot 10^{-3}$ mol dm^{-3} of **1b** in 0.1 M Bu_4NPF_6/MeCN on a glassy carbon disk working electrode (d = 1.7 mm) at a potential scan rate of 100 mV·s^{-1} (*top*) and 25, 50, 100, 200, 500 and 1000 mV·s^{-1} (*bottom*). Temperature 298 K.

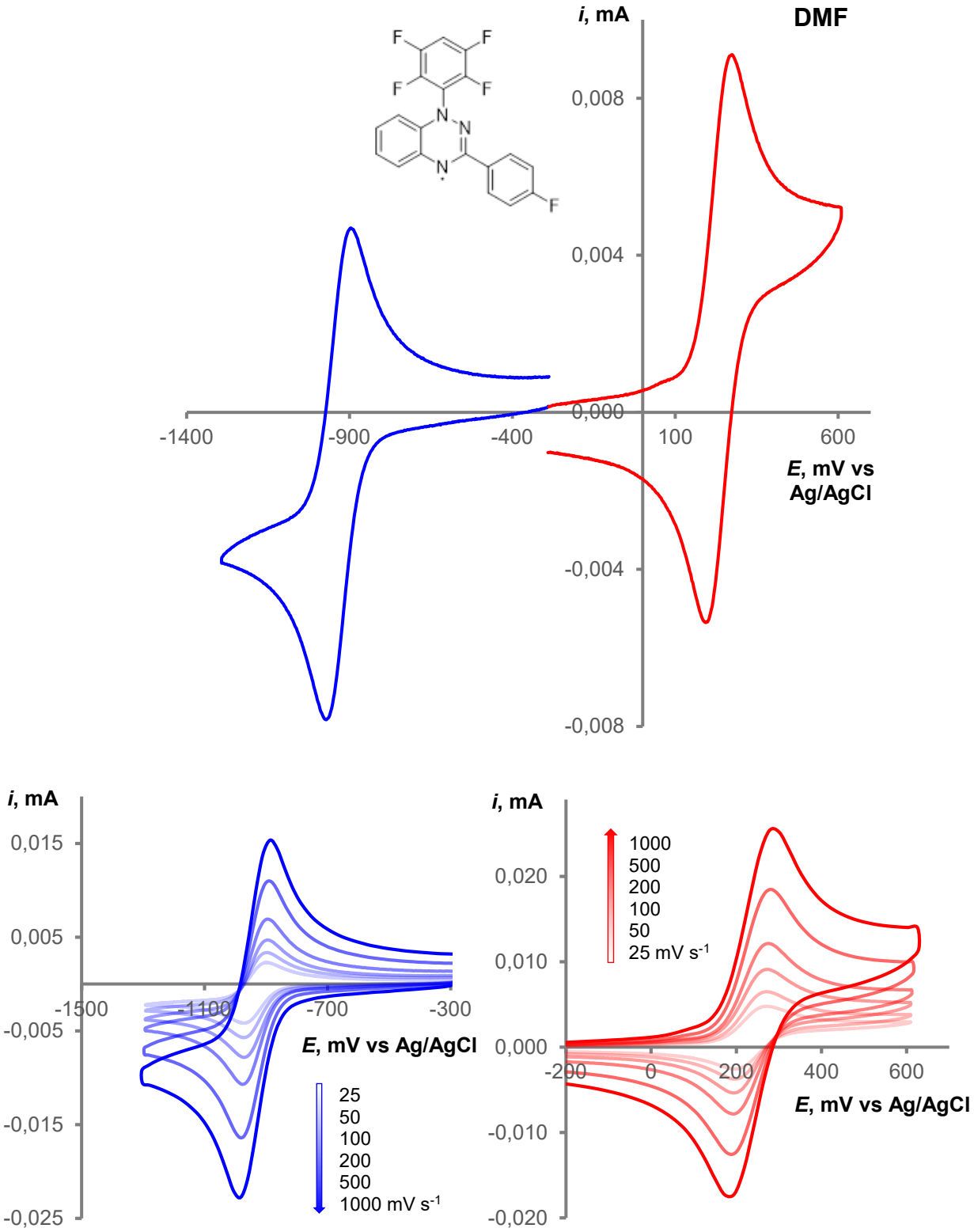

Figure S9. CV curves of reduction (*blue*) and oxidation (*red*) of $1 \cdot 10^{-3}$ mol dm^{-3} of **1b** in 0.1 M Bu_4NPF_6/DMF on a glassy carbon disk working electrode (d = 1.7 mm) at a potential scan rate of 100 mV·s^{-1} (*top*) and 25, 50, 100, 200, 500 and 1000 mV·s^{-1} (*bottom*). Temperature 298 K.

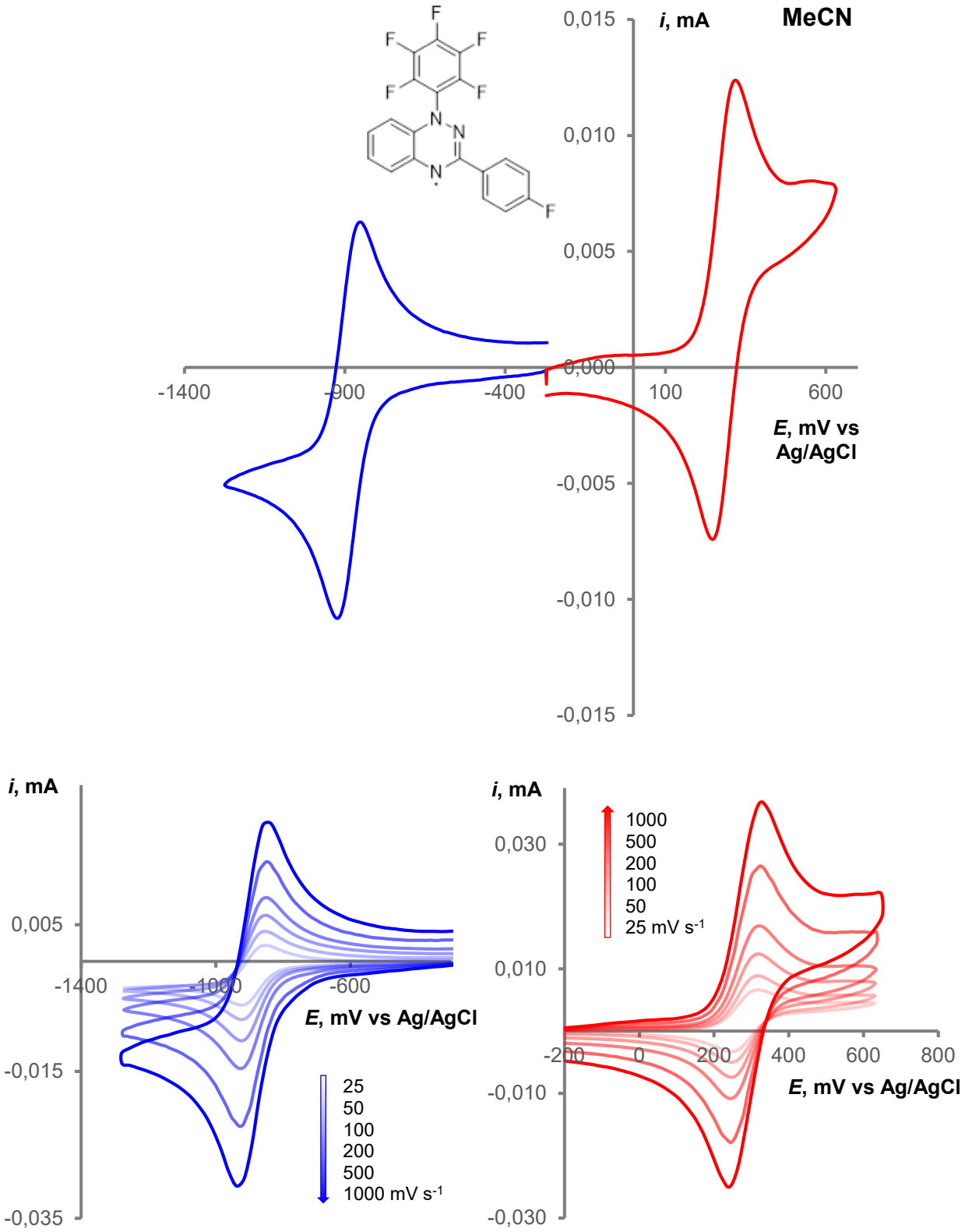

Figure S10. CV curves of reduction (*blue*) and oxidation (*red*) of $1.5 \cdot 10^{-3}$ mol·dm^{-3} of **1c** in 0.1 M Bu_4NPF_6/MeCN on a glassy carbon disk working electrode (d = 1.7 mm) at a potential scan rate of 100 mV·s^{-1} (*top*) and 25, 50, 100, 200, 500 and 1000 mV·s^{-1} (*bottom*). Temperature 298 K.

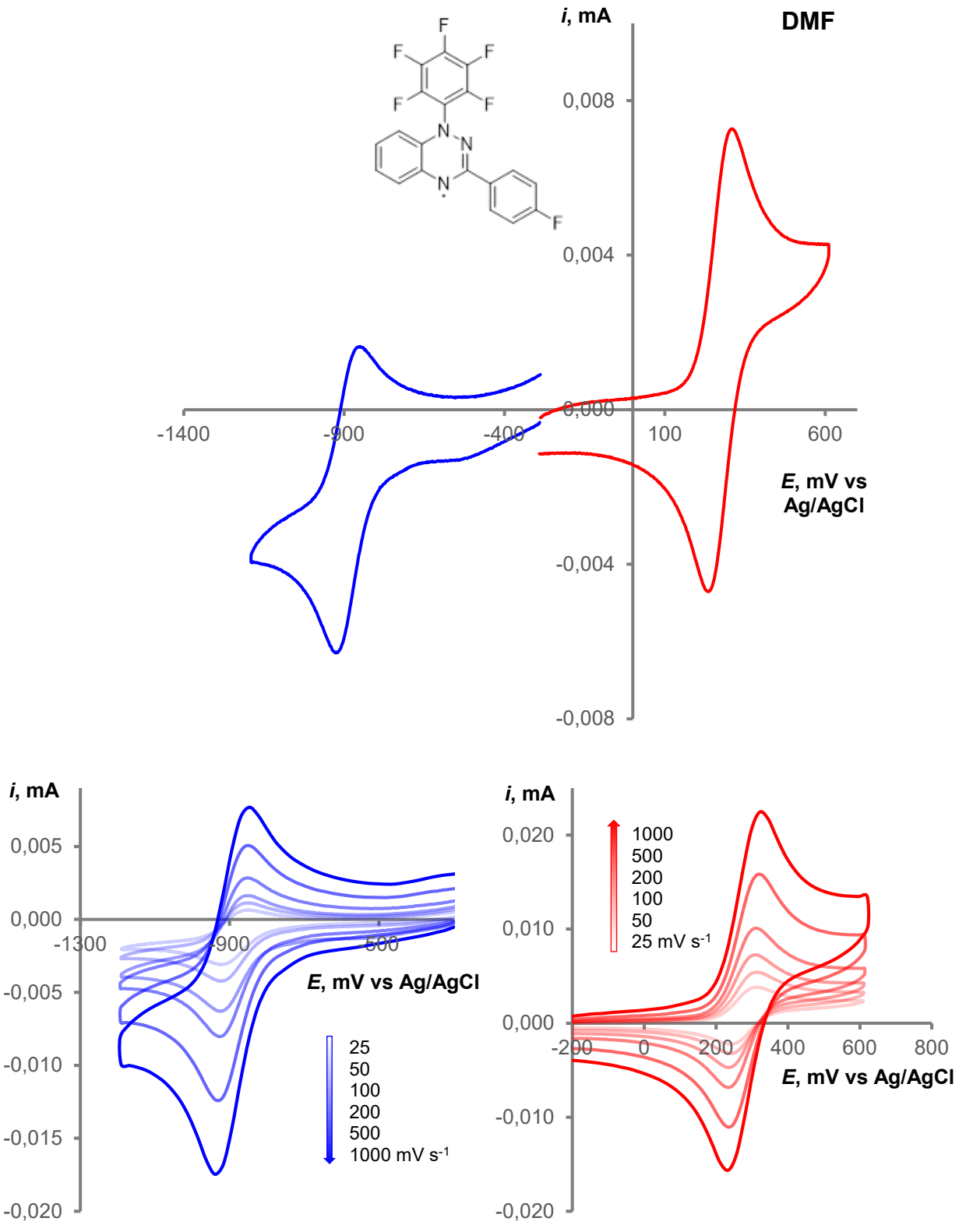

Figure S11 CV curves of reduction (*blue*) and oxidation (*red*) of $1 \cdot 10^{-3}$ mol·dm^{-3} of **1c** in 0.1 M Bu_4NPF_6/DMF on a glassy carbon disk working electrode (d = 1.7 mm) at a potential scan rate of 100 mV·s^{-1} (*top*) and 25, 50, 100, 200, 500 and 1000 mV·s^{-1} (*bottom*). Temperature 298 K.

UV-Vis Spectra

The UV-Vis absorption spectra of the studied compounds are shown in Figure S12.

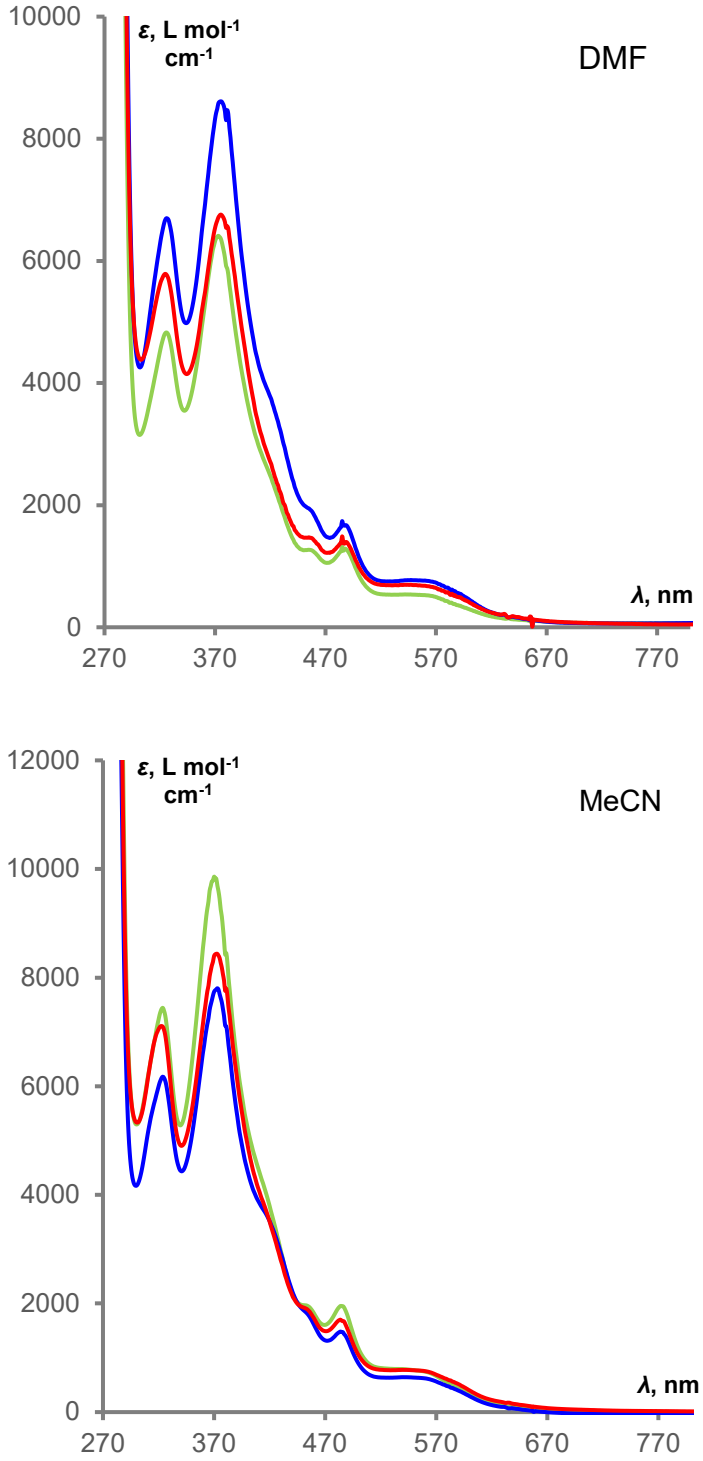

Figure S12. UV-vis spectra of $2 \cdot 10^{-4}$ mol·dm^{-3} solutions of compounds **1a** (*green*), **1b** (*blue*) and **1c** (*red*) in DMF (*top*) and MeCN (*bottom*).

EPR Spectra

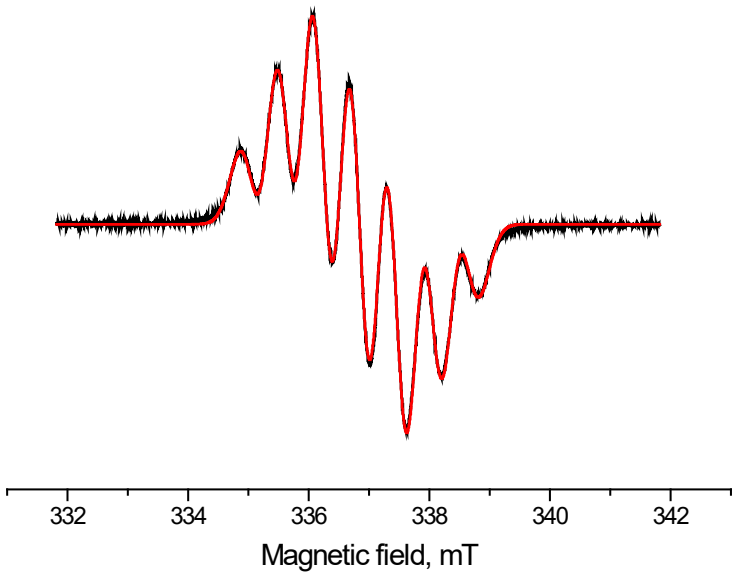

Figure S13. Experimental (black) and simulated (red) EPR spectra for a degassed ~10^{-5} M solution of **1b** in toluene at 298 K, spectrum modeled with A1(N)=0.56 mT, A2(N)=0.52 mT, A3(N)=0.68 mT

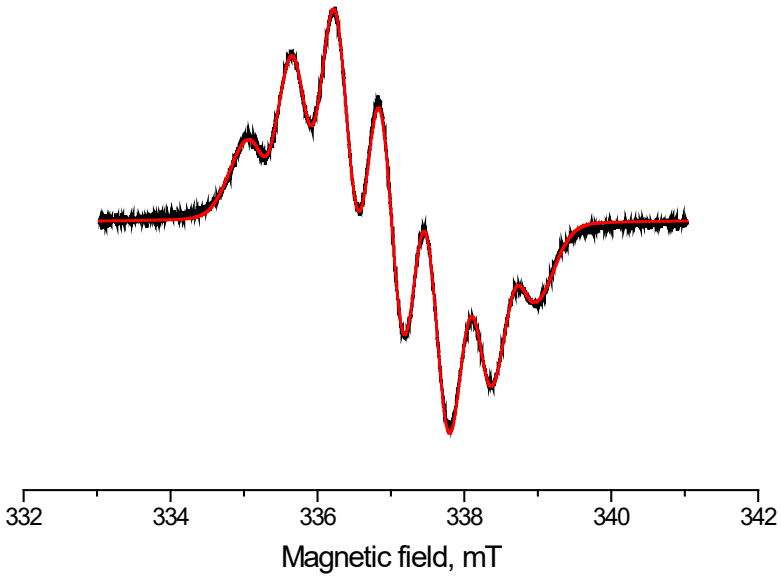

Figure S14. Experimental (black) and simulated (red) EPR spectra for a degassed ~10^{-5} M solution of **1c** in toluene at 298 K, spectrum modeled with A1(N)=0.57 mT, A2(N)=0.53 mT, A3(N)=0.68 mT

Results of DFT Calculations

Parameters (J) of the pair exchange interactions ($\hat{H} = -2J\hat{\vec{S}}_1\hat{\vec{S}}_2$) between radicals **1a**, **1b** and **1c** were calculated using the spin-unrestricted broken-symmetry approach[S6] at the BS-B3LYP/def2-TZVP level,[S7-S9] using the Yamaguchi formula:[S10]

$$J = -\frac{E^{HS} - E_{BS}^{LS}}{\langle S^2\rangle^{HS} - \langle S^2\rangle_{BS}^{LS}}.$$

This approach has previously been shown to work well for evaluating intermolecular exchange interactions.[S11,S12] The spin population of nitrogen atoms, hyperfine coupling constants (*hfcc*) and g-tensors were calculated at the UPBE0/def2-TZVP level.[S13] For all calculations, the ORCA 5.0.5 software package was used.[S14]

Figure S15 shows that the spin density is localized mainly in the triazinyl core and predominantly (86%) on nitrogen atoms. The highest population is observed for N_4 and is independent of the degree of fluorination. Therefore, J parameter calculations were performed for all types of radical pairs in the crystal structure at a distance of less than 10 Å between N atoms in position 4 of the radicals. At larger distances between atoms with high spin population of neighboring radicals, the magnitude of the exchange interaction is negligible (at the level of numerical accuracy of the calculations or less).

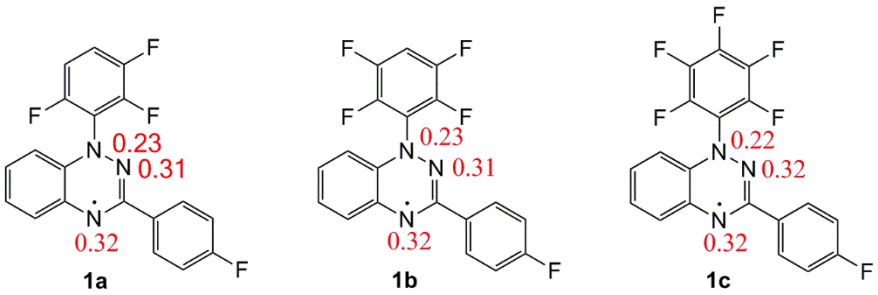

Figure S15. Spin population of the nitrogen atoms (in red) of the radicals **1a** – **1c** calculated at the UPBE0/def2-TZVP level.

As mentioned in the main text, the unit cell of crystals **1a** and **1b** contains four crystallographically independent molecules, and the unit cell of **1c** contains two crystallographically independent molecules. Nevertheless, BS-UB3LYP calculations predicted two types of strongly untiferromagnetically coupled radical pairs (or dimers with $|J| > 50\ cm^{-1}$) for all crystals **1a**, **1b** and **1c**. Figure S16 shows these pairs for **1a**; the structures of these dimers are similar and the J parameters for them are also very close (198 and 185 cm^{-1}, Table S4). Apart from these two dimers, there are also 6 other different types of pairs with prominent exchange interaction (10 $cm^{-1} > |J| > 2\ cm^{-1}$). Figure S17 shows two pairs with moderate antiferromagnetic exchange interaction (J = –9.5 and –8.5 cm^{-1}), whose parameters are about 20 times smaller than those of the previous dimers. It can be noted that all the above pairs consist of molecules of the different types (**1a**A···**1a**B, **1a**C···**1a**D). Thus, the magnetic motif in crystals of radical **1a** consists of two types of strongly AF-coupled radical dimers with much weaker AF interactions between them. However, since the parameters J for these dimers are very close (a difference of only 7%), the simulation of the temperature dependence of the magnetic susceptibility for **1a** should be performed assuming a simplified magnetic motif consisting of one type of AF coupled dimers (the Bleaney–Bowers model).

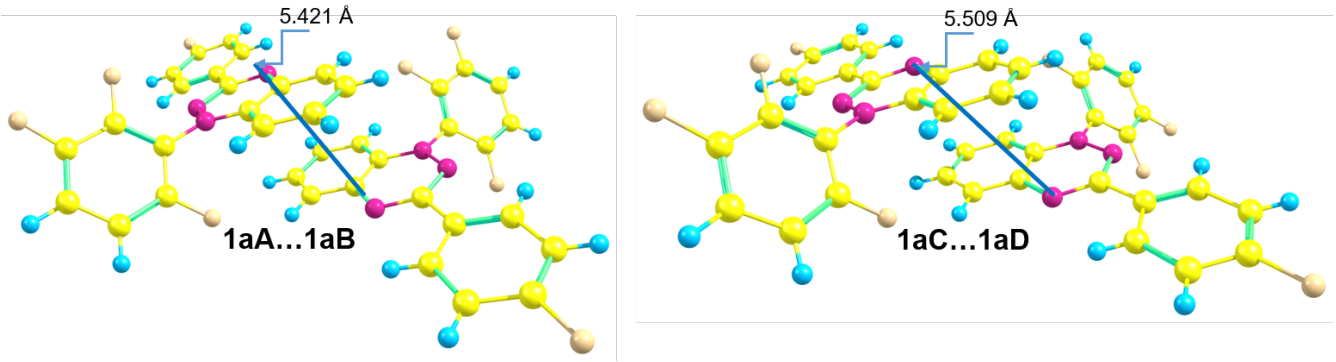

Figure S16. Two types of strongly exchange-coupled dimers **1a**A···**1a**B (left) and **1a**C···**1a**D (right) with the shortest intermolecular N(4)···N(4) distances indicated by blue lines.

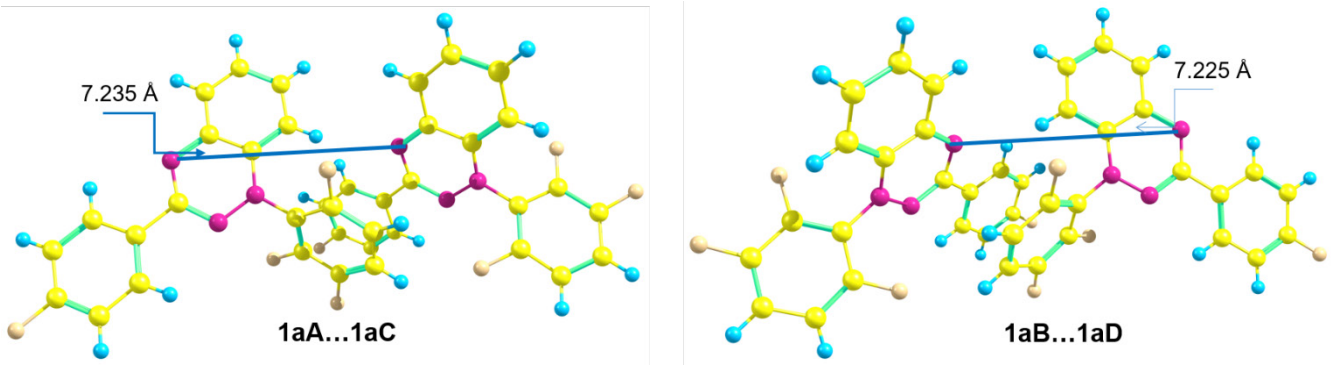

Figure S17. Two types of exchange-coupled dimers **1a**A···**1a**C (left) and **1a**B···**1a**D (right) with the intermolecular N(4)···N(4) distances indicated by blue lines.

Figure S18 shows the strongly antiferromagnetically coupled pairs for **1b**. The structures of these dimers are also similar, but the shortest N(4)···N(4) distances differs for them more significantly (by 0.22 Å) than in **1a** (0.09 Å). Thus, the *J* parameters for them differ significantly (–120 and –169 cm^{-1}, Table S4). Thus, the magnetic motif in crystals of **1b** consists of two types of strongly AF-coupled radical dimers with much weaker AF interactions between them.

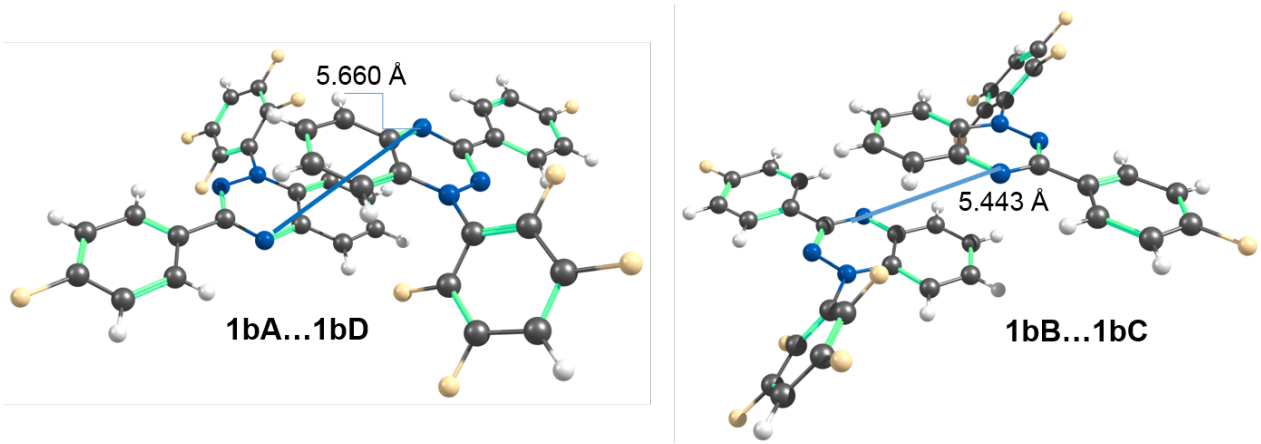

Figure S18. Two types of strongly exchange-coupled dimers **1b**A···**1b**D (left) and **1b**B···**1b**C (right) with the shortest intermolecular N(4)···N(4) distances indicated by blue lines.

Figure S19 shows the strongly antiferromagnetically coupled pairs for **1c**. As in the case of **1a** and **1b**, the structures of these dimers are also similar, with the shortest N(4)···N(4) distances differing even more considerably (by 0.42 Å) than in **1b** (0.22 Å). Therefore, the *J* parameters for them also differ more strongly (–158 and –54 cm^{-1}, Table S4). Thus, the magnetic motif in crystals of **1c** consists of two types of strongly AF-coupled radical dimers with much weaker AF interactions between them.

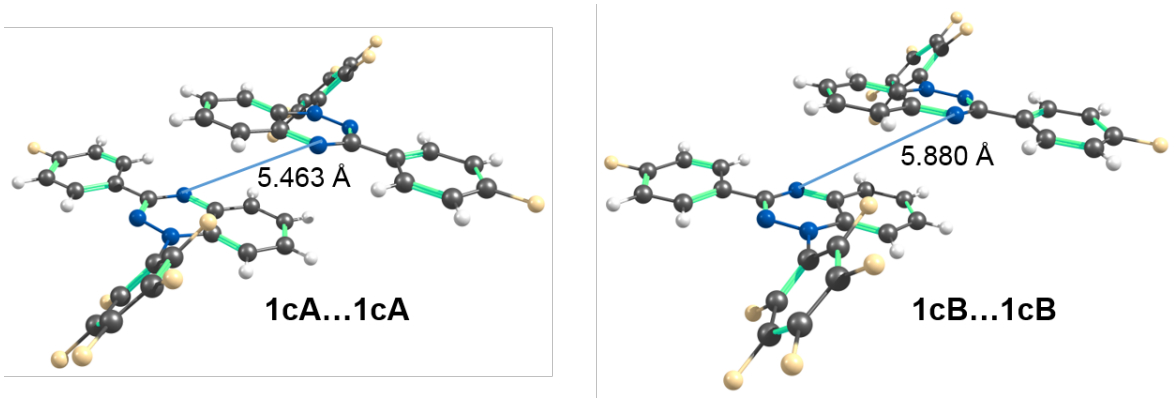

Figure S19. Two types of strongly exchange-coupled dimers **1c**A···**1c**A (left) and **1c**B···**1c**B (right) with the shortest intermolecular N(4)···N(4) distances indicated by blue lines.

Table S4. Characteristic structural features and calculated and best-fit exchange interaction parameters for crystals of the Blatter radical series **1a**, **1b** and **1c**.

Radical	Structure motif	Pairs	R_{min}(N(4)···N(4))	J, cm^{-1} (J/k_B, K)	
				Calculated	Best-fit
1a	One type of antiferromagnetically-coupled dimers	**1a**A···**1a**B	5.421	**–198 (–285)**	**–125 ± 2 (–180 ± 3)**
		1aC···**1a**D	5.509	**–185 (–266)**	
		1aA···**1a**B	8.609	+2.6	g = 2.11 ± 0.01
		1aC···**1a**D	8.643	+2.3	p = 1.0%
		1aA···**1a**C	7.235	–9.5	
			7.306	–9.6	
		1aB···**1a**D	7.225	–8.5	
			7.232	–8.6	
1b	Two types of antiferromagnetically-coupled dimers	**1b**A···**1b**D	5.660	**–120 (–173)**	**–105.6 ± 1.5 (–152± 2)**
		1bB···**1b**C	5.443	**–169 (–243)**	**–129 ± 2 (–185± 3)**
		1aA···**1a**C	7.167	–8.94	g = 2.11±0.01
		1aA···**1a**C	7.235	–8.24	p = 0.9%
		1bB···**1b**D	7.211	–8.2	
		1bB···**1b**D	7.257	–9.3	
1c	Two types of antiferromagnetically-coupled dimers	**1c**A···**1c**A	5.463	**–158 (–227)**	**–113 ± 5 (–163 ± 7)**
		1cB···**1c**B	5.880	**–54 (–78)**	**–36.1 ± 1.5 (–52 ± 2)**
		1cA···**1c**A	8.265	–3.8	g = 2.04 ± 0.03
		1cB···**1c**B	8.500	+4.1	p = 2.9%
		1cA···**1c**B	7.147	–4.6	
		1cA···**1c**B	7.235	–3.9	

Simulation of Temperature Dependences of Magnetic Susceptibility

The magnetic susceptibility of **1a**–**c** was measured using a Quantum Design MPMS*XL* SQUID magnetometer in the temperature range 2−300 K in a magnetic field up to 5 kOe. It was corrected for the diamagnetic contribution.

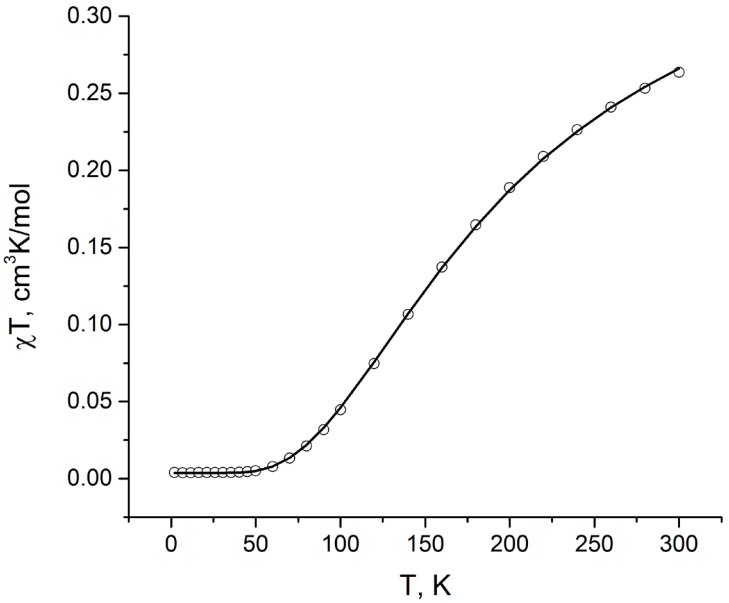

Figure S20. Temperature dependence of χT product for radical **1a** (open circles). Solid line is simulation for a magnetic motif consisting of a fraction of non-interacting radicals (p) and a fraction p of radicals forming antiferromagnetically coupled dimers with the following parameters: $J = -125 \pm 2$ cm^{-1} ($J/k_B = -180 \pm 3$ K), $g = 2.11 \pm 0.01$, $p = 0.01$.

The temperature dependences of the paramagnetic susceptibility (χ) for radicals **1a**–**1c** were simulated using the home-made Spinner program (https://github.com/ruthenium96/spinner) and the magnetic motifs predicted by the above BS-DFT calculations. For **1a**, a simplified magnetic motif consisting of one type of AF coupled dimers was used (Figure S16). Figure S20 shows that very good agreement between simulation and experiment is observed, with the best-fit parameter $J/k_B = -180 \pm 3$ K being in reasonable agreement with the calculations (266 and 285 K).

Results of simulation for **1b** are presented in the main text (Figure 4), and they also demonstrate good agreement between experiment and calculations. Figure S21 shows the product χT *vs* T dependence for radical **1c**. In general, there is also a good agreement between experiment and simulation, but with a noticeable difference at T< 25 K. The best-fit parameters J_1/k_B = −163 ± 7 K and J_2/k_B = −52 ± 2 K are also in good agreement with calculations (227 and 78 K).

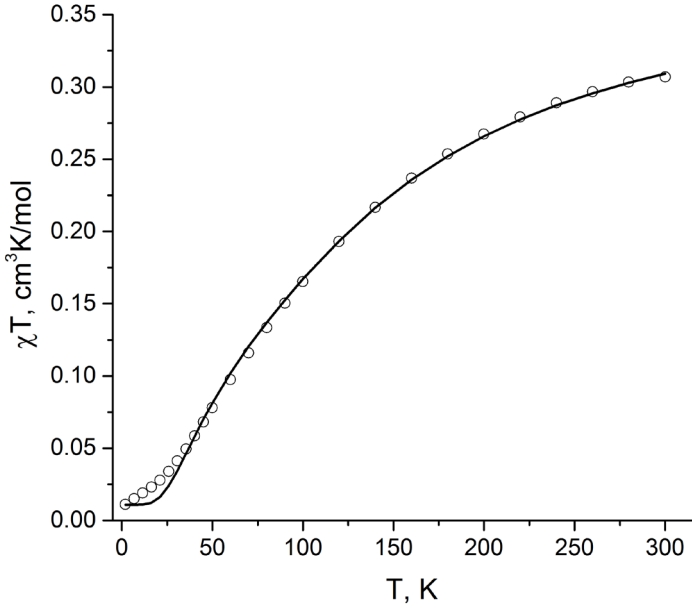

Figure S21. Temperature dependence of χT product for radical **1c** (open circles). Solid line is simulation for a magnetic motif consisting of a fraction of non-interacting radicals (p) and a fraction p of radicals forming two types of antiferromagnetically coupled dimers with the following parameters: J_1 = −113 ± 5 cm^{-1} (J_1/k_B = −163 ± 7 K), J_2 = −36.1 ± 1.5 cm^{-1} (J_2/k_B = −52 ± 2 K), g = 2.04 ±0.03, p = 0.029.

High-Resolution Mass Spectrometry Data

Acquisition Parameter

Source Type	ESI	Ion Polarity	Positive	Set Nebulizer	0.4 Bar
Focus	Not active			Set Dry Heater	180 °C
Scan Begin	50 m/z	Set Capillary	4500 V	Set Dry Gas	4.0 l/min
Scan End	3000 m/z	Set End Plate Offset	-500 V	Set Divert Valve	Waste

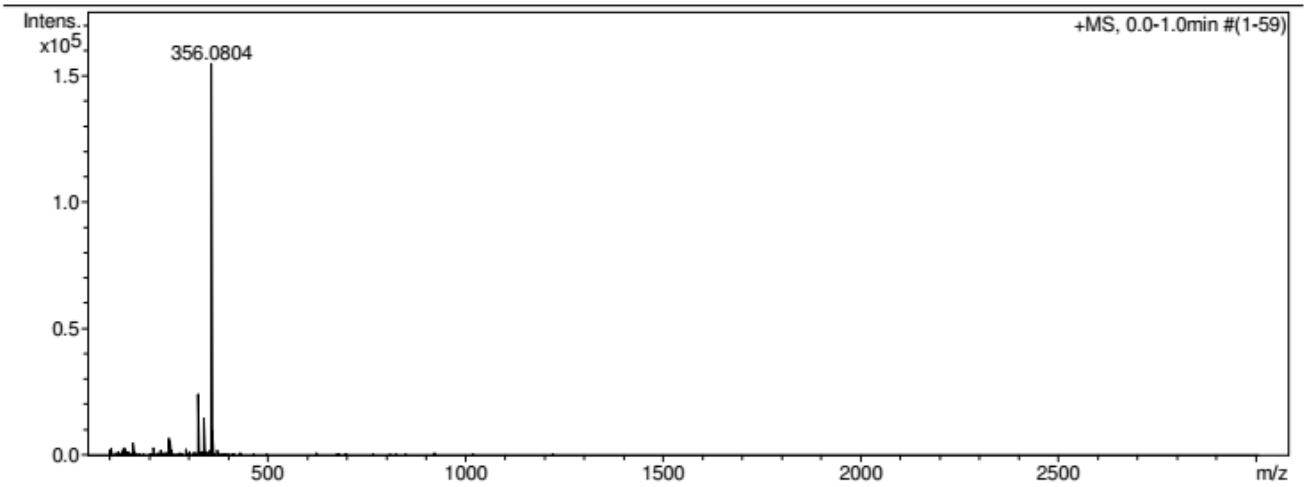

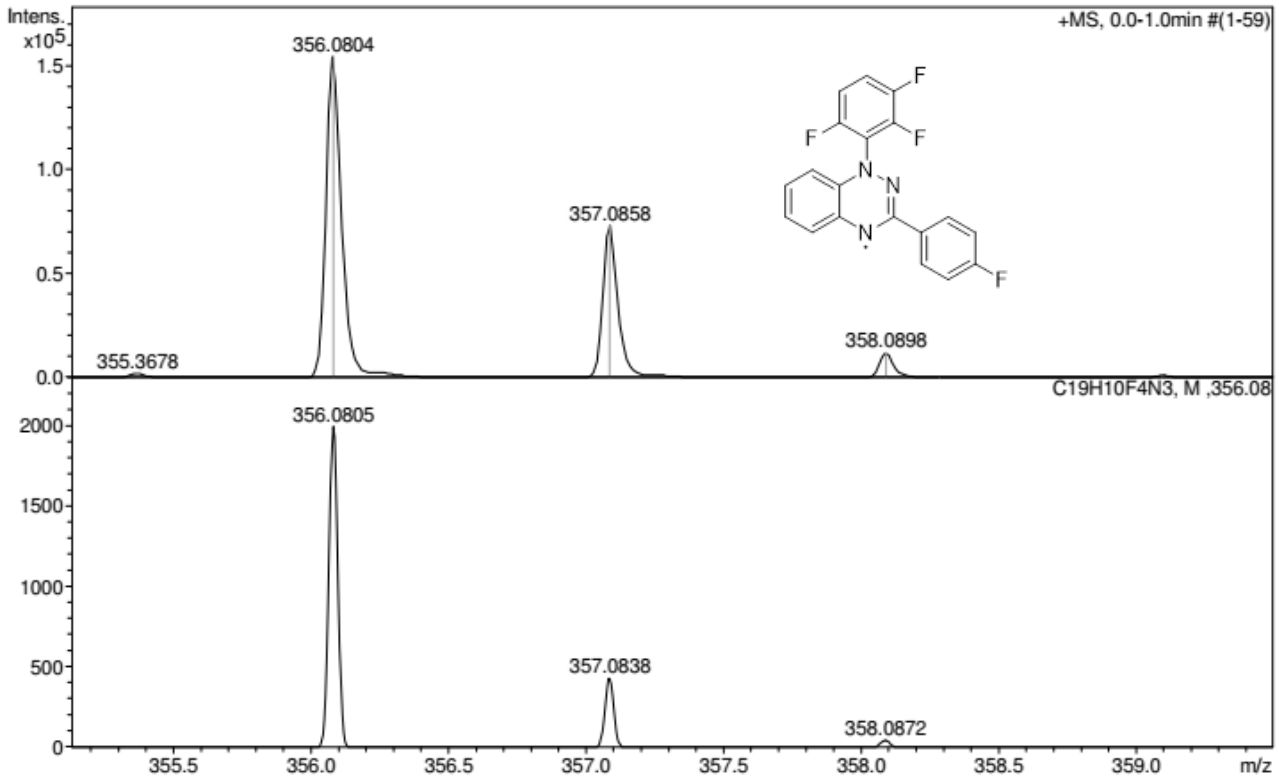

Acquisition Parameter

Source Type	ESI	Ion Polarity	Positive	Set Nebulizer	0.4 Bar
Focus	Not active			Set Dry Heater	180 °C
Scan Begin	50 m/z	Set Capillary	4500 V	Set Dry Gas	4.0 l/min
Scan End	3000 m/z	Set End Plate Offset	-500 V	Set Divert Valve	Waste

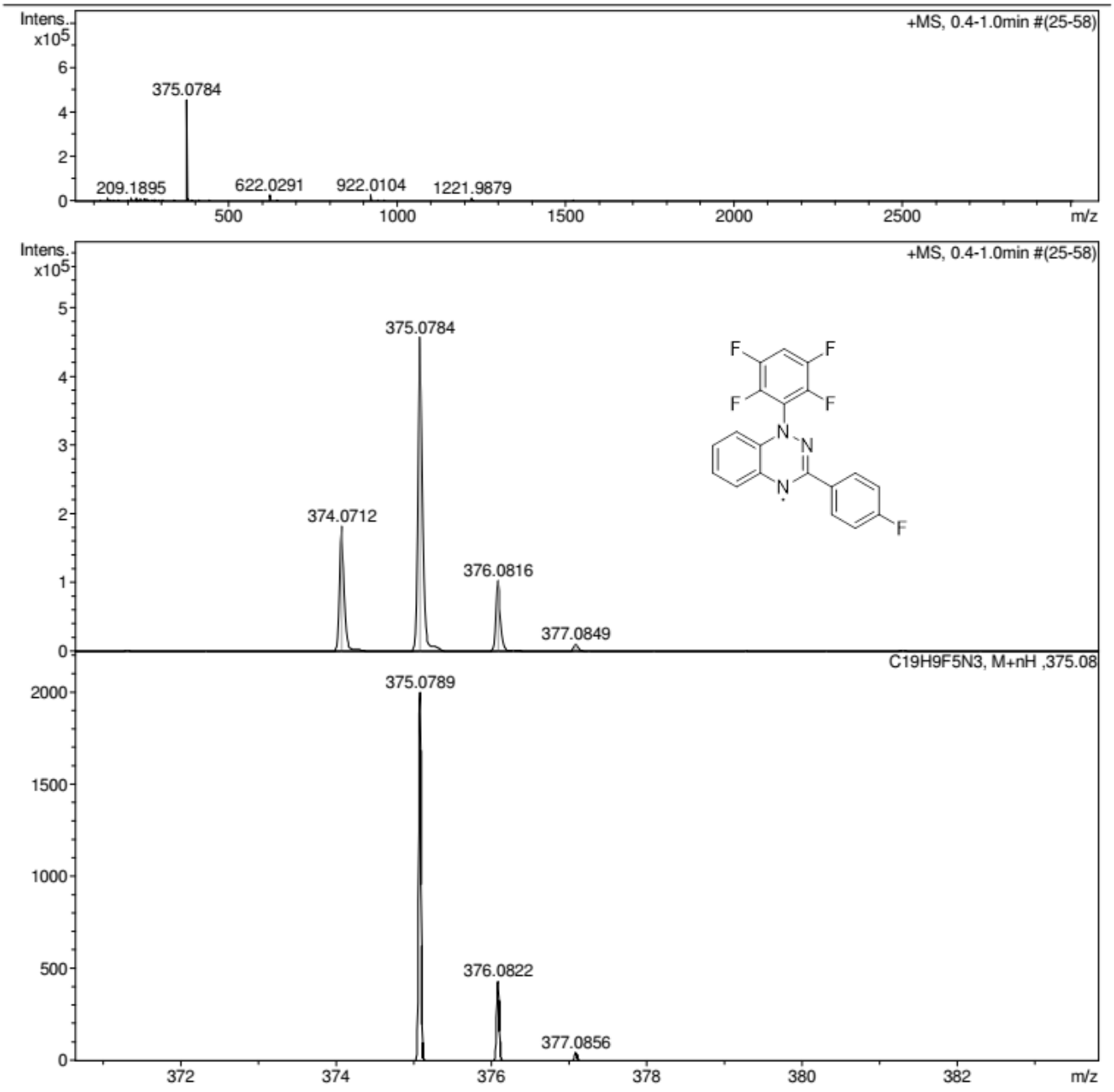

Acquisition Parameter

Source Type	ESI	Ion Polarity	Positive	Set Nebulizer	0.4 Bar
Focus	Not active			Set Dry Heater	180 °C
Scan Begin	50 m/z	Set Capillary	4500 V	Set Dry Gas	4.0 l/min
Scan End	3000 m/z	Set End Plate Offset	-500 V	Set Divert Valve	Waste

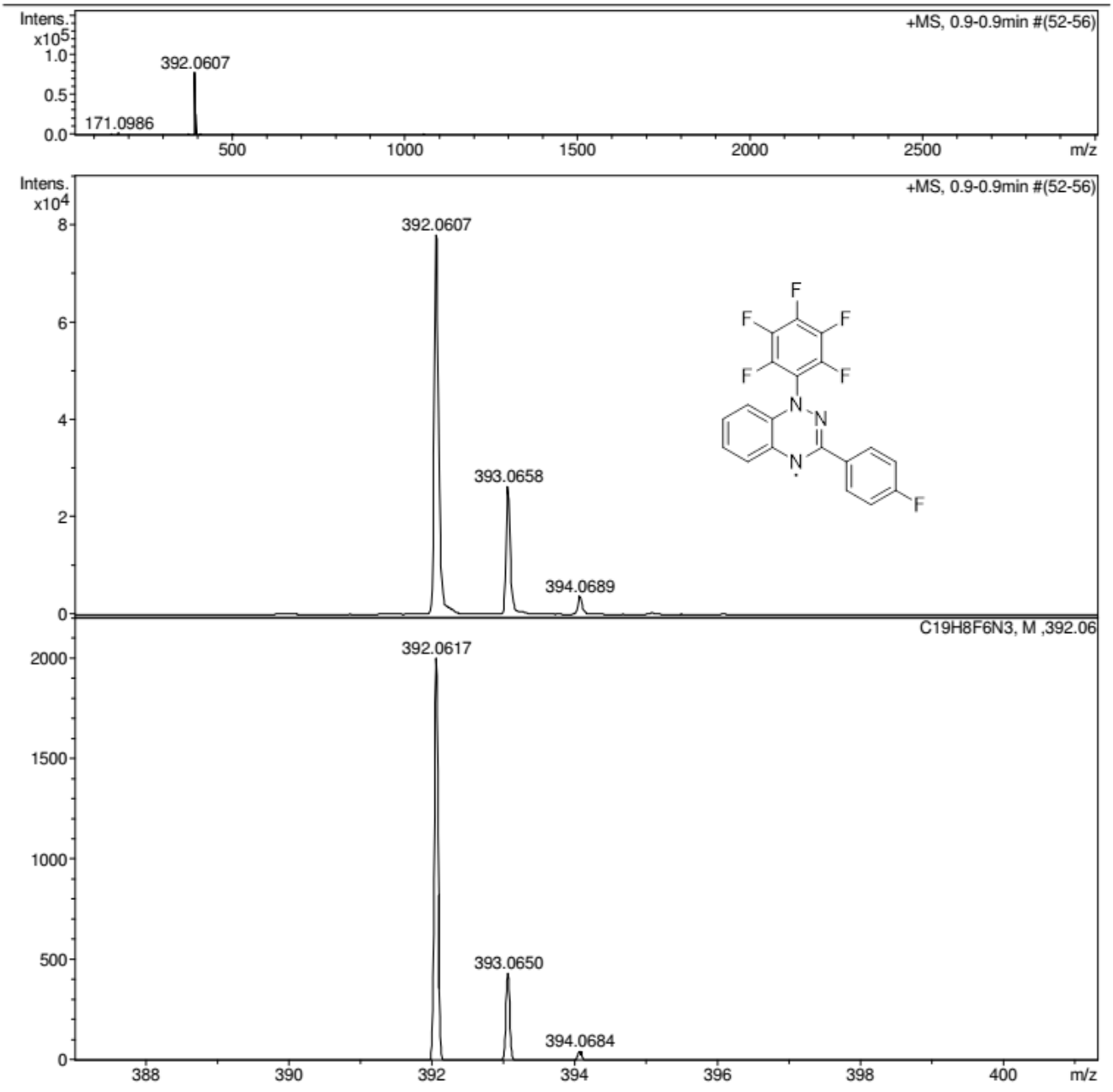

IR Spectra

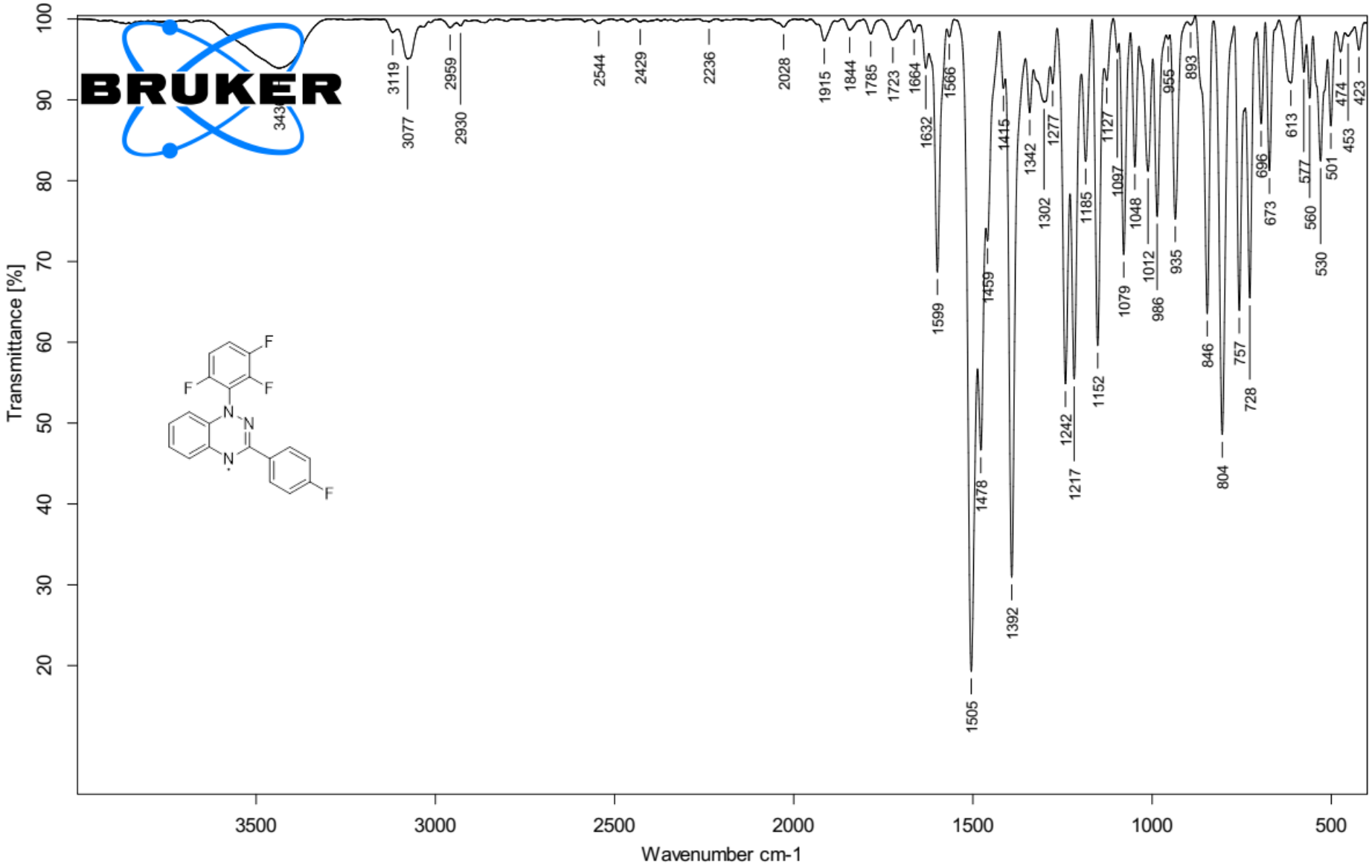
BRUKER
Transmittance [%]
100
90
80
70
60
50
40
30
20
3500
3000
2500
2000
1500
1000
500
Wavenumber cm-1
3119
3077
2959
2930
2544
2429
2236
2028
1915
1844
1785
1723
1664
1632
1599
1566
1505
1478
1459
1415
1392
1342
1302
1277
1242
1217
1185
1152
1127
1097
1079
1048
1012
986
955
935
893
846
804
757
728
696
673
613
577
560
530
501
474
453
423
F
F
F
N
N
N
F

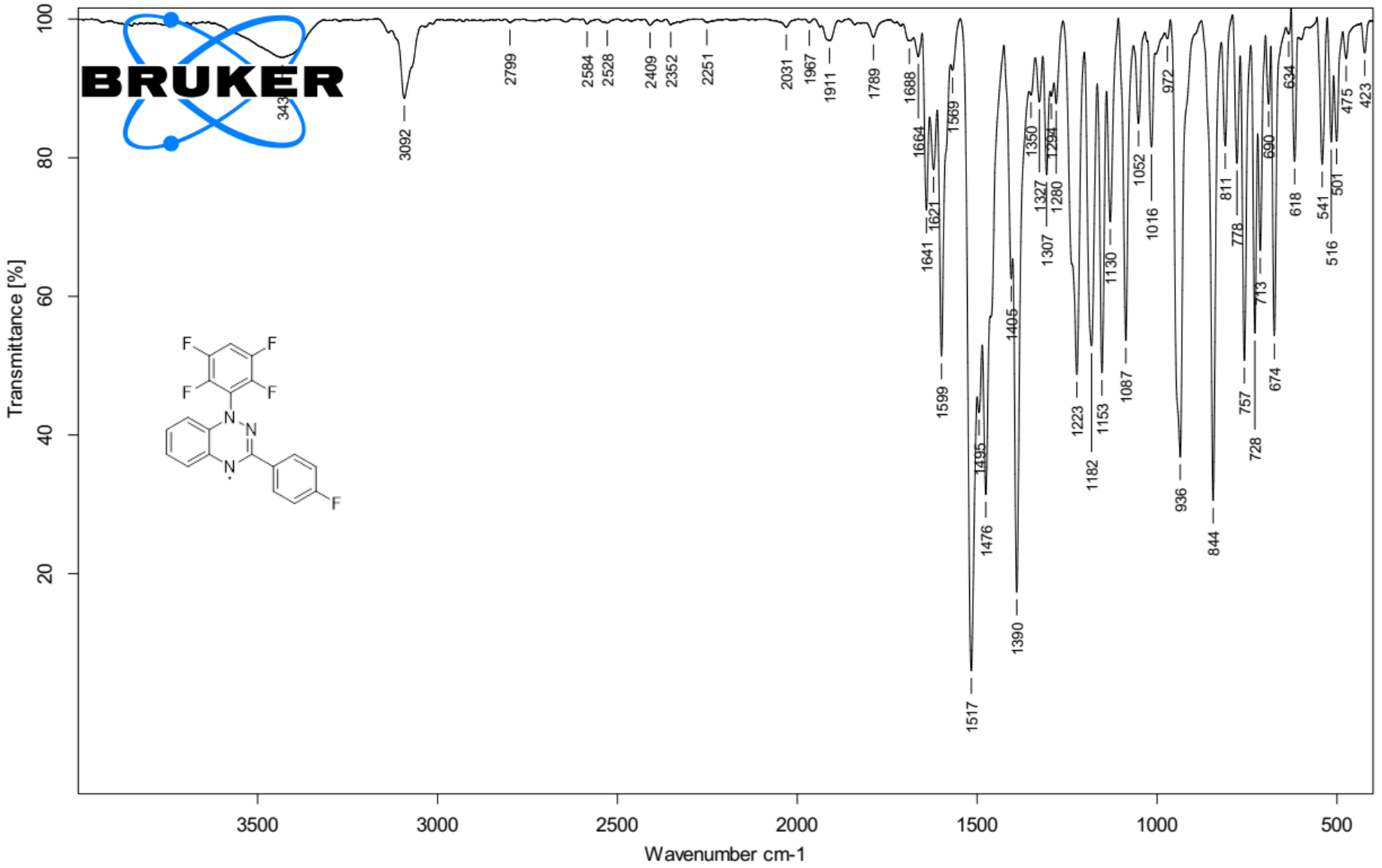
BRUKER
Transmittance [%]
100
80
60
40
20
3500
3000
2500
2000
1500
1000
500
Wavenumber cm-1
3431
3092
2799
2584
2528
2409
2352
2251
2031
1967
1911
1789
1688
1664
1641
1621
1599
1569
1517
1495
1476
1405
1390
1350
1327
1307
1294
1280
1223
1182
1153
1130
1087
1052
1016
972
936
844
811
778
757
728
713
690
674
634
618
541
516
501
475
423
F
F
F
F
N
N
N
F

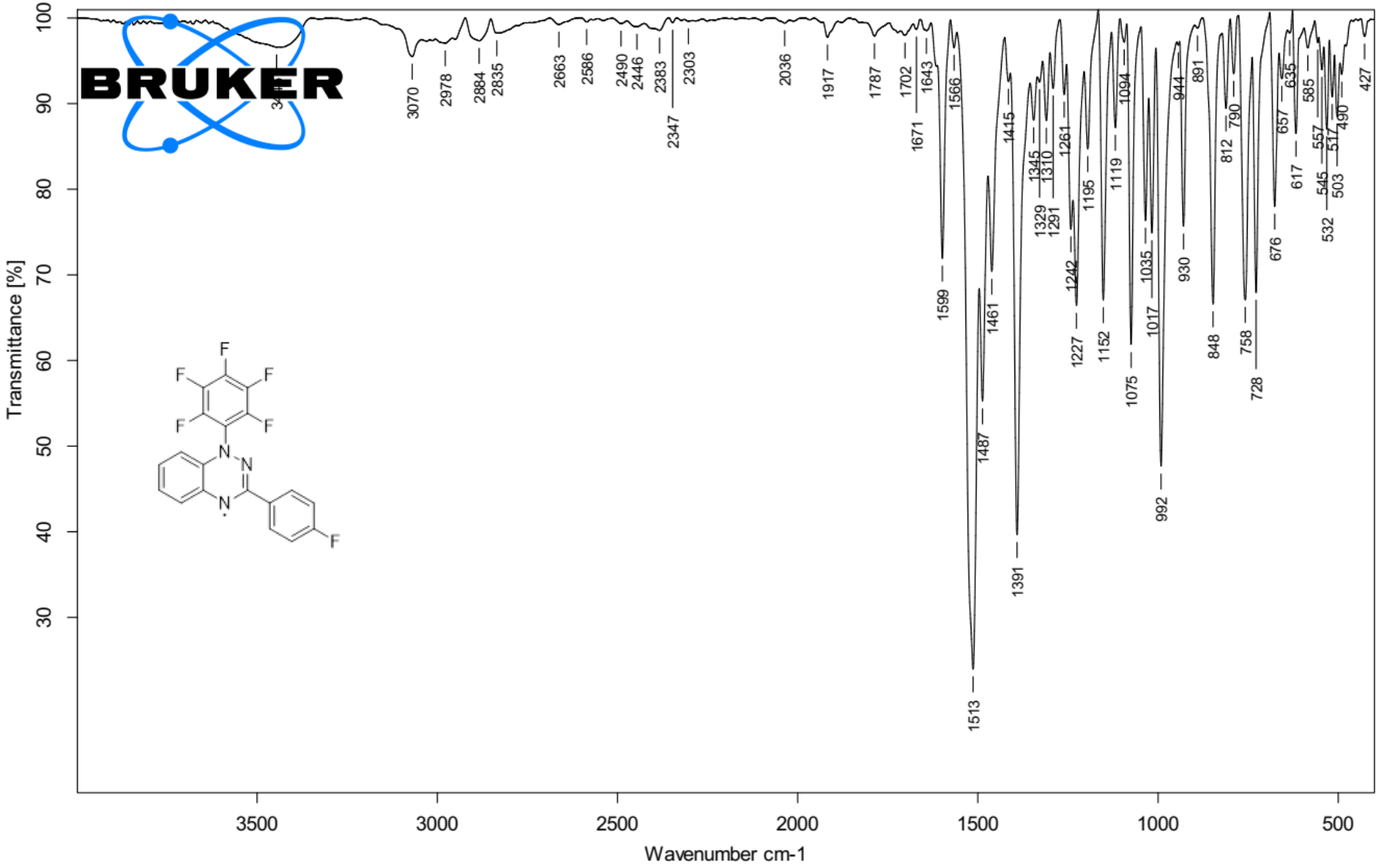
BRUKER
Transmittance [%]
Wavenumber cm-1
3500
3000
2500
2000
1500
1000
500
100
90
80
70
60
50
40
30
3411
3070
2978
2884
2835
2663
2586
2490
2446
2383
2347
2303
2036
1917
1787
1702
1671
1643
1599
1566
1513
1487
1461
1415
1391
1345
1329
1310
1291
1261
1242
1227
1195
1152
1119
1094
1075
1035
1017
992
944
930
891
848
812
790
758
728
676
657
635
617
585
557
545
532
517
503
490
427
F
F
F
F
F
N
N
N
F

References

S1. *APEX3, RLATT, CELL_NOW, TWINABS, SAINT-Plus and SADABS*, Bruker AXS, Madison, WI, USA, 2016.

S2. L. Krause, R. Herbst-Irmer, G. M. Sheldrick and D. Stalke, *J. Appl. Crystallogr*., 2015, **48**, 3; https://doi.org/10.1107/S1600576714022985.

S3. G. M. Sheldrick, *Acta Crystallogr*., 2015, **A71**, 3; https://doi.org/10.1107/S2053273314026370.

S4. G. M. Sheldrick, *Acta Crystallogr*., 2015, **C71**, 3; https://doi.org/10.1107/S2053229614024218.

S5. O. V. Dolomanov, L. J. Bourhis, R. J. Gildea, J. A. K. Howard and H. Puschmann, *J. Appl. Crystallogr*., 2009, **42**, 339; https://doi.org/10.1107/S0021889808042726.

S6. H. Nagao, M. Nishino, Y. Shigeta, T. Soda, Y. Kitagawa, T. Onishi, Y. Yoshika and K. Yamaguchi, *Coord. Chem. Rev*., 2000, **198**, 265; https://doi.org/10.1016/S0010-8545(00)00231-9.

S7. A. D. Becke, *J. Chem*. *Phys.*, 1993, **98**, 5648; https://doi.org/10.1063/1.464913.

S8. C. Lee, W. Yang and R. G. Parr, *Phys. Rev. B*, 1988, **37**, 785; https://doi.org/10.1103/PhysRevB.37.785.

S9. F. Weigend and R. Ahlrichs, *Phys. Chem. Chem. Phys.*, 2005, **7**, 3297; https://doi.org/10.1039/B508541A.

S10. T. Soda, Y. Kitagawa, T. Onishi, H. Nagao, Y. Yoshioka and K. Yamaguchi, *Chem. Phys. Lett*., 2000, **319**, 223; https://doi.org/10.1016/S0009-2614(00)00166-4.

S11. E. V. Tretyakov, V. I. Ovcharenko, A. O. Terent'ev, I. B. Krylov, T. V. Magdesieva, D. G. Mazhukin and N. P. Gritsan, *Russ. Chem. Rev*., 2022, **91**, RCR5025; https://doi.org/10.1070/RCR5025.

S12. E. V. Tretyakov, P. V. Petunin, S. I. Zhivetyeva, D. E. Gorbunov, N. P. Gritsan, M. V. Fedin, D. V. Stass, R. I. Samoilova, I. Yu. Bagryanskaya, I. K. Shundrina, A. S. Bogomyakov, M. S. Kazantsev, P. S. Postnikov, M. E. Trusova and V. I. Ovcharenko, *J. Am. Chem. Soc*., 2021, **143**, 8164; https://doi.org/10.1021/jacs.1c02938.

S13. C. Adamo and V. Barone, *J. Chem. Phys.*, 1999, **110**, 6158; https://doi.org/10.1063/1.478522.

S14. F. Neese, *Wiley Interdiscip. Rev.:Comput. Mol. Sci*., 2022, **12**, e1606; https://doi.org/10.1002/wcms.1606.